

# Likelihood distribution for models with cosmological constant from COBE data

Marco Tucci<sup>1,2</sup>, Angela Contaldo<sup>1</sup>, Silvio Bonometto<sup>2,3</sup>

## ABSTRACT

Using COBE–DMR 4–year data, we find a general expression yielding the likelihood distribution in the 3–dimensional parameter space spanned by the spectral index  $n$ , the spectral amplitude  $a_{10}$  and the false–vacuum density parameter  $\Omega_\Lambda$ . Using such simple expression, the range of possible normalizations, within a given likelihood interval from top–likelihood normalization, is readily found, with fair approximation, for any model with total density parameter  $\Omega_o = 1$  and assigned  $n$  and  $\Omega_\Lambda$ .

*Subject headings:* cosmic microwave background – cosmology: theory – dark matter – large–scale structure of the Universe – methods: numerical

## 1. Introduction

The COBE–DMR data, so far, provide the only all–sky map for the cosmic microwave background radiation (CMBR) (Smoot et al. 1992). Using such data, the angular temperature fluctuation spectrum  $C_l$  can be inspected for  $l$  values from 2 to 30. In principle, cosmological model parameters should be adjusted so to provide the best possible fit to all  $C_l$ . Unfortunately, however, the situation is more complicated than so. As a matter of fact, model independent  $C_l$  values and error bars were provided by Hinshaw et al. (1996), Bunn & White (1997), Tegmark & Hamilton (1997), assuming that  $l(l+1)C_l$  takes single values, in suitable  $l$  intervals. Tegmark (1997) and Górski (1997) also provided angular spectrum data and error bars, separately for all  $l$  values. Attempting to use such  $C_l$  to fix model parameters, as outlined also by Górski (1997), is far from trivial. In fact, two main difficulties arise. First of all, each  $C_l$  distribution, around its maximum likelihood value, is not Gaussian, as is witnessed by its non–symmetric  $1\sigma$  error bars; deviations from a Gaussian behaviour are

even stronger beyond  $1\sigma$ . Furthermore, the  $C_l$  estimators are strongly correlated with each other. Therefore, even obtaining the likelihood distribution for each  $C_l$ , up to a few  $\sigma$ 's around their maximum likelihood values, a simultaneous direct fit to different  $C_l$ 's bears no clear statistical significance. Then, if precise likelihood comparisons within a given class of models are to be made, one has little alternative to fitting directly model parameters to COBE–DMR pixel data. Such data are however public and can be found on the NASA site (<http://space.gsfc.nasa.gov/astro/cobe/>).

In this work we focused on models with total density parameter  $\Omega_o = 1$ , due to contributions of baryons (density parameter  $\Omega_b$ ), cold–dark–matter (CDM; density parameter  $\Omega_c$ ), and false vacuum (density parameter  $\Omega_\Lambda = \Lambda/8\pi G\rho_{cr}$ ). Recent outputs of BOOMERanG and Maxima I experiment (de Bernardis et al. 2000, Hanany et al. 2000) confirm that  $\Omega_o$  values substantially different from unity are disfavoured.  $\Omega_c$  and  $\Omega_\Lambda$ , together with the primeval spectrum index  $n$  and the primeval spectrum normalization, are the parameters which mostly shape the  $C_l$  spectrum. On the contrary, up to  $l \simeq 30$ , the dark–matter (DM) composition and the Hubble constant  $H$  bear a limited impact only. Attention was recently concentrated on models with  $\Lambda \neq 0$ , mostly because data on SN Ia (Riess et al. 1998, Perlmutter et

<sup>1</sup>Physics Department, Università degli Studi di Milano, Milano (Italy)

<sup>2</sup>I.N.F.N., Via Celoria 16, I20133 Milano (Italy)

<sup>3</sup>Physics Department G. Occhialini, Università degli Studi di Milano–Bicocca, Milano (Italy)

al. 1999) seem to favour a negative deceleration parameter.

Previous analyses of the likelihood distribution in the  $a_{10}$ - $n$  plane were performed by various authors. The parameter  $a_{10} = \sqrt{C_{10}} T_0$  accounts for primeval spectrum normalization in a simple way, as its best-fitting value is nearly independent of  $n$  in the 4-year COBE data.

Assuming a pure Sachs & Wolfe spectrum (Sachs & Wolfe 1967, Bond & Efstathiou 1987), Górski et al. (1994), Bennet et al. (1994), Wright et al. (1994), Bond (1995) and Tegmark & Bunn (1995) analysed the 2-year COBE data. Under the same assumption, Górski et al. (1996, G96 hereafter), Bennet et al. (1996), Wright et al. (1996) and Hinshaw et al. (1996), analysed the 4-year COBE data. Such spectrum can be considered a reasonable approximation for pure CDM or mixed models with  $\Omega_o = 1$ , for low  $l$ 's. On the contrary, open or  $\Lambda$  models are expected to behave differently (see, e.g., Stompor & Górski 1994). A first attempt to determine the normalisation of  $\Lambda$  models and an upper limit on the density parameter  $\Omega_\Lambda$  using the 2-year COBE data was performed by Stompor, Górski & Banday (1995a, b) and Bunn & Sugiyama (1995). But the most extended results on the likelihood of  $\Lambda$ -models, based on 4-year COBE data, were obtained by Bunn & White (1997, BW hereafter).

Let us briefly summarize BW results, which were also partially included in the popular CMB-FAST code (Seljak & Zaldarriaga 1996), to show why a further effort is needed to complete them. BW define a function  $D(x) = l(l+1)C_l$ , with  $x = \log_{10} l$ , so that  $D(1) = 110 C_{10}$ , and consider the parameters  $D'$  and  $D''$  in the expansion

$$D(x) \simeq D_1 \left[ 1 + D'(x-1) + \frac{D''}{2}(x-1)^2 \right]. \quad (1)$$

Accordingly,  $D'$  and  $D''$  essentially account for the first and second derivative of  $D(x)$  at  $x = 1$  ( $l = 10$ ). BW provide, also through an analytic fitting expression, the maximum-likelihood normalization  $D_1$  for models defined by the values of  $D'$ ,  $D''$  parameters and the likelihood distribution in  $D'$ - $D''$  plane, for the top likelihood value of  $D_1$ . Among 2-parameter fittings of COBE-DMR data, the BW approach is quite effective in treating  $\Lambda$ -models, as fixing  $D'$  and  $D''$  corresponds to giving  $n$  and  $\Lambda$  and *viceversa*.

However, BW provide only a partial information on the likelihood of models whose amplitude is close to (but not coincident with) the best-fit amplitude for given  $n$ . In fact, let  $\bar{n}-\bar{a}_{10}$  yield the top-likelihood model and  $n_{\pm} = \bar{n} \pm \Delta n$  limit the  $1\sigma$  error bar along the  $n$  axis, as given by BW. They complete the information on likelihood distribution, by stating that  $1\sigma$  error bars (on amplitude) roughly correspond to 7%.

In order to determine the likelihood of a model defined by  $n$ - $a_{10}$  values close to  $\bar{n}-\bar{a}_{10}$ , one has to assume that, at least within  $1\sigma$ , the likelihood distribution is Gaussian. If so, one may determine first the likelihood of the intermediate model given by  $n-\bar{a}_{10}$ . Then, still assuming a Gaussian distribution along the  $a_{10}$  axis, one may determine the further likelihood decrease when passing from  $n-\bar{a}_{10}$  to  $n-a_{10}$ . As a matter of fact, both distributions, along the  $n$  and the  $a_{10}$  axes, are significantly non-Gaussian, as is shown by the shape itself of the top-likelihood curve. This already affects the above procedure within  $1\sigma$ , but makes it seriously unadequate above  $1\sigma$ .

It may be important, instead, to know how the likelihood is distributed among models with different normalizations. For instance, varying the normalization of a model with given  $n$  and  $\Lambda$ , we may predict different galaxy cluster number densities. A model under-(over-)producing clusters, for maximum-likelihood normalization, might be in agreement with observations if a different normalization is taken. If this occurs for spectral index and normalization within  $1\sigma$  from the top-likelihood values  $\bar{n}-\bar{a}_{10}$ , rejecting such model because of cluster predictions is illegitimate. But also knowing the range of normalizations allowed, within 1-2-3  $\sigma$ 's, for a model with given  $\Lambda$  and  $n$  may be relevant, as well as determining, for a given  $n$  and normalization, which is the range of  $\Lambda$  values allowed at the 1-2-3  $\sigma$  level. Similar arguments can be made for the capacity of a model to predict a fair amount of high- $z$  objects or to fit the spectral slope parameter  $\Gamma$ , yielding the ratio between mass variances at 8 and 25  $h^{-1}$ Mpc (see, e.g., Bonometto & Pierpaoli 1998, for more details), while other parameter combinations may also have to be explored.

Quite in general, to extend BW results in this way, we must perform a 3-parameter analysis of COBE-DMR data. Our parameters are the spec-

tral index  $n$ , the normalization  $a_{10}$ , and the vacuum density parameter  $\Omega_\Lambda$ . The result of our analysis will be a handable analytic expressions of the likelihood distribution in such 3-parameter space. We shall also provide a simple numerical routine, which can be appended to CMBFAST and gives, besides of the best-fit normalization for fixed  $n$  and  $\Lambda$ , also the limits of the fluctuation amplitude intervals where likelihood decrements corresponding to  $n$   $\sigma$ 's ( $n = 1, 2, 3$ ) occur. Other details provided by such routine will be discussed below.

## 2. From COBE data to the likelihood distribution

In this section we shall report how the likelihood distribution is obtained from COBE-DMR data. A large part of this section is based on Górski (1994, G94 hereafter). Its details are unessential to read the following sections and to use our relations yielding the likelihood distribution. Let us rather draw the reader's attention on the Appendix B, where we show in detail how the likelihood dependence on monopole and dipole terms are integrated out.

COBE-DMR temperature data were estimated at the frequencies of 31.5, 53, and 90 GHz. Using such estimates, the vectors  $\mathbf{d}$ , with  $N_p$  (pixel number) components  $d_i$ , can be built. The signal variance, due to uncertainties of instrumental origin at each pixel,  $\sigma_i$ , can also be collected in  $N_p$ -dimensional *noise* vectors ( $\boldsymbol{\sigma}$ ). Each pixel is centered on a point of the celestial sphere of coordinates  $\hat{n}_i \equiv (\theta_i, \phi_i)$ . The likelihood of a given model  $\mathcal{M}$  is obtained by comparing  $\mathbf{d}$  with a *fictitious data* vector  $\boldsymbol{\delta}$  (components  $\delta_i$ ), built from the model, but taking into account how real data are obtained and, therefore, also the noise vector  $\boldsymbol{\sigma}$ . Noise correlation among pixels, expected to be small, will be neglected in our theoretical developments.

In principle this can be done by evaluating the matrix  $\mathbf{M}$ , whose components

$$M_{ij} = \langle \delta_i \delta_j \rangle \quad (2)$$

are obtained by averaging on the ensemble of  $\mathcal{M}$  realizations. Assuming a Gaussian statistics, the likelihood of  $\mathcal{M}$  reads then:

$$\mathcal{L} = [(2\pi)^{N_p} \det \mathbf{M}]^{-1/2} \exp[-(1/2) \mathbf{d}^T \mathbf{M}^{-1} \mathbf{d}] . \quad (3)$$

A slight non-Gaussian behaviour in data (Ferreira, Maguejo & Górski 1998, Novikov, Feldman & Shandarin 1998, Pando, Valls-Gabaud & Fang 1998) possibly originated by post-recombination processes, should not affect our analysis, as shown in detail by Contaldi et al. (1999), for a standard CDM model.

However, eq. (3) can hardly be used, because of the high dimensionality of the matrix  $\mathbf{M}$ , which should be inverted. Replacing the pixel basis (a discretized coordinate representation) by an angular harmonic basis (essentially its Fourier transform) allows to reduce the dimensionality of matrices, without wasting physical information. When doing so, we must also take into account that temperature fluctuation data about the galactic equatorial plane do not give cosmological information.

In order to evaluate the likelihood of a model  $\mathcal{M}$ , therefore, the first step amounts to defining the set of real spherical harmonics:

$$Y_{lm}(\hat{r}) = \sqrt{l+1/2} \sqrt{\frac{(l-|m|!)}{(l+|m|!)}} P_l^{|m|}(\cos \theta) f_m(\phi) \quad (4)$$

where

$$f_m(\phi) = (2\pi)^{-1/2}, \pi^{-1/2} \cos(m\phi), \pi^{-1/2} \sin(|m|\phi) \quad (5)$$

for  $m = 0, > 0, < 0$ , respectively, while the

$$P_l^m(x) = (-1)^m (1-x^2)^{m/2} (d/dx)^{|m|} P_l(x) \quad (6)$$

are obtained by differentiating the ordinary Legendre polynomials  $P_l$ . Such spherical harmonics are built so to fulfill the orthonormality conditions

$$\int_{4\pi} d^2 \hat{r} Y_{lm}(\hat{r}) Y_{l'm'}(\hat{r}) = \delta_{ll'} \delta_{mm'} \quad (7)$$

when the integration is extended on the whole sky. If this integration is replaced by a sum on the  $N_p$  pixel centers, orthonormality is recovered by replacing  $Y_{lm}$  by

$$\hat{Y}_{lm}(\hat{r}) = w_l^{pix} Y_{lm}(\hat{r}) \quad (8)$$

(a table of  $w_l^{pix}$  and directions on their computation are given in Appendix A).

Using such spherical harmonics, then, we can build the components of a fictitious signal vector,

for the point  $\hat{r}_i$ , yielding the  $i$ -th pixel, as follows:

$$\delta(\hat{r}_i) = \sum_{l=0}^{\infty} \sum_{m=-l}^l (a_{lm}^{CMB} w_l^{DMR} + a_{lm}^{\text{noise}}) \hat{Y}_{lm}(\hat{r}_i). \quad (9)$$

Here, besides of  $a_{lm}^{CMB}$ , that are to be obtained for a realization of  $\mathcal{M}$ , we need the  $a_{lm}^{\text{noise}}$  originated by the instrumental noise and the window function  $w_l^{DMR}$  for the observational apparatus (given, e.g., by Wright et al. 1994). Accordingly, as above outlined, the fictitious signal vector that we shall build will convolve the features of a given cosmology with the characteristics of the COBE-DMR apparatus.

It is also convenient to put together the indices  $l$  and  $m$ , by defining

$$\mu = l(l+1) + (m+1). \quad (10)$$

If  $l$  values up to  $l_{max} = 30$  are considered,  $\mu$  attains the maximum value  $\mu_{max} = (l_{max} + 1)^2 = 961$ . Accordingly, the functions  $\hat{Y}_{\mu}$  define the passage from the  $N_p$ -dimensional pixel basis to a 961-dimensional basis. In the sequel, latin indices shall be used to indicate vector components on the pixel basis only; accordingly, eq. (9) can be unambiguously rewritten as

$$\delta_i = \sum_{\mu} (\tilde{a}_{\mu}^{CMB} + a_{\mu}^{\text{noise}}) \hat{Y}_{\mu i} \quad (11)$$

( $\sim$  is used to indicate that window function effects are already taken into account).

Let us then remind that the  $a_{lm}^{CMB} \equiv a_{\mu}^{CMB}$ , that we shall build, depend on the model  $\mathcal{M}$  and on its realization; ensemble averaging them, one would obtain the angular spectrum components  $C_l \equiv \langle |a_{lm}^{CMB}|^2 \rangle$ .

The use of spherical harmonics, however, gives place to a problem. When using real data, pixels within  $20^\circ$  from the galactic plane are to be excluded (in the sequel, residual pixels will be said to belong to the *cut-sky*). First of all, this reduces  $N_p$  from 6144 to 4016. Furthermore, in the cut sky, the set of polynomials  $\hat{Y}_{\mu}$  is no longer orthonormal. Orthonormality, however, can be recovered by replicing the basis  $\hat{\mathbf{Y}} \equiv \{\hat{Y}_{\mu}\}$  by the basis

$$\mathbf{\Psi} = \mathbf{\Gamma} \cdot \hat{\mathbf{Y}}$$

where  $\mathbf{\Gamma}$  is a  $961 \times 961$  matrix that we shall now define. In order to have  $\langle \mathbf{\Psi} \mathbf{\Psi}^T \rangle_{c.s.} = \mathbf{I}$  ( $\langle \dots \rangle_{c.s.}$  is

a product obtained summing on the set of pixels belonging to the cut-sky;  $\mathbf{I}$  is the unit matrix), it must be

$$\mathbf{\Gamma} \cdot \langle \hat{\mathbf{Y}} \hat{\mathbf{Y}}^T \rangle_{c.s.} \cdot \mathbf{\Gamma}^T = \mathbf{I} \quad (12)$$

and this is obtained if the matrix  $\langle \hat{\mathbf{Y}} \hat{\mathbf{Y}}^T \rangle_{c.s.}$  is expressed as a product  $\mathbf{L} \cdot \mathbf{L}^T$  and

$$\mathbf{\Gamma} = \mathbf{L}^{-1}. \quad (13)$$

Here we shall use the upper-triangular matrix  $\mathbf{\Gamma}$ , obtained by performing the so-called Koleski decomposition, as done by G94. This choice is not unique; alternative possibilities are discussed by Tegmark (1997). However, as we shall see, this choice allows a simple integration of the likelihood on monopole and dipole data.

The fictitious data vector  $\boldsymbol{\delta}$ , can be expanded on both  $\mathbf{Y}$  and  $\mathbf{\Psi}$  bases; let  $\tilde{a}_{\mu}$  and  $c_{\mu}$  be its components, respectively. Clearly:

$$\tilde{a}_{\mu} = \sum_{\nu} \Gamma_{\mu\nu} c_{\nu} \quad \text{and} \quad c_{\mu} = \sum_{\nu} L_{\mu\nu} \tilde{a}_{\nu}. \quad (14)$$

Therefore, once Koleski decomposition provides the  $\mathbf{L}$  matrix, we readily obtain  $c_{\mu} = \langle \mathbf{d} \mathbf{\Psi}_{\mu} \rangle_{c.s.}$ ; in particular, besides of the CMB component  $c_{\mu}^{CMB}$ , the noise component  $c_{\mu}^{\text{noise}}$  is soon obtainable. Let us also outline that, thanks to the triangular form of the  $\mathbf{L}$  matrix, the  $c_{\mu}$  coefficients are linear combinations of  $a_{\nu}$  coefficients with  $\nu \geq \mu$ .

Using the basis  $\mathbf{\Psi}_{\mu}$ , eq. (11) reads:

$$\delta_i = \sum_{\mu} c_{\mu} \Psi_{\mu i} = \sum_{\mu} (c_{\mu}^{CMB} + c_{\mu}^{\text{noise}}) \Psi_{\mu i} \quad (15)$$

and

$$\begin{aligned} M_{\mu\nu} &= \langle c_{\mu} c_{\nu} \rangle = \langle c_{\mu}^{CMB} c_{\nu}^{CMB} \rangle + \langle c_{\mu}^{\text{noise}} c_{\nu}^{\text{noise}} \rangle \\ &= M_{\mu\nu}^{CMB} + M_{\mu\nu}^{\text{noise}} \end{aligned} \quad (16)$$

is the new correlation matrix (assuming that signal and noise are both distributed in a Gaussian way and uncorrelated). Using  $M_{\mu\nu}^{CMB}$  and  $M_{\mu\nu}^{\text{noise}}$ , the expression for the likelihood of the model reads:

$$\begin{aligned} \mathcal{L} &= [(2\pi)^N \det(\mathbf{M}^{CMB} + \mathbf{M}^{\text{noise}})]^{-1/2} \times \\ &\times \exp[-(1/2) \mathbf{c}^T (\mathbf{M}^{CMB} + \mathbf{M}^{\text{noise}})^{-1} \mathbf{c}]. \end{aligned} \quad (17)$$

Here  $\mathbf{c}$  is a vector with 961 components  $c_{\mu}$ . Thanks to the triangular form of  $\mathbf{L}$ , we can easily integrate the likelihood results on  $c_{\mu}$  for  $\mu = 1, \dots, 4$

(such integration can be made in an exact way; details are given in Appendix B). Hence, in the cut sky, the effective basis dimensionality will be 957 (for each signal frequency to be considered).

To build the likelihood eq. (17),  $\tilde{C}_l$  are obtained using the CMBFAST program, convolved with the COBE–DMR window function. Then, according to eq. (14),

$$\mathbf{M}^{CMB} = \mathbf{L}^T \cdot \langle \tilde{\mathbf{a}}^{CMB} \tilde{\mathbf{a}}^{CMB T} \rangle \cdot \mathbf{L} = \mathbf{L}^T \cdot \mathbf{C}^{CMB} \cdot \mathbf{L}; \quad (18)$$

here  $\mathbf{C}^{CMB}$  is a diagonal matrix, whose diagonal terms are the components of the angular spectrum  $\tilde{C}_l$ , however is repeated  $2l+1$  times (for all  $\mu$  values which correspond to a given  $l$ ).  $\mathbf{M}^{CMB}$  is then to be set together with the noise matrix

$$\mathbf{M}^{\text{noise}} = \langle \mathbf{c}^{\text{noise}} \mathbf{c}^{\text{noise T}} \rangle = \Omega_{pix}^2 \sigma_i^2 \Psi_i \Psi_i^T \quad (19)$$

(the index  $i$  runs on the 4016 pixels of the cut-sky).

In this way, the likelihood of a given model  $\mathcal{M}$  is finally evaluated and different models may be tested against COBE–DMR data.

### 3. Results

Using the approach described in the previous section, substantially coincident with G94 treatment, we considered a lattice of models for  $h$  varying from 0.5 to 0.7 and  $\Omega_\Lambda$  from 0 to 0.8. For each model, the likelihood was evaluated for different values of  $n$  and  $a_{10}$ . We used 4-year COBE–DMR data, performing a weighted average of 53 and 90 GHz outputs; we verified that using the noisy data at 31.5 GHz does not add any substantial improvement. More precisely, in accordance with Tegmark & Bunn (1995) and Bunn & White (1997), we may set

$$d_i = \frac{d_i(53)\sigma_i^{-2}(53) + d_i(90)\sigma_i^{-2}(90)}{\sigma_i^{-2}(53) + \sigma_i^{-2}(90)} \quad (20)$$

and

$$\sigma_i^{-2} = \sigma_i^{-2}(53) + \sigma_i^{-2}(90) \quad (21)$$

as data and noise vector components, respectively. Using such inputs, we worked out the 3-dimensional curves  $\mathcal{L}(n, a_{10})$  for each model. As an example, in Fig. 1 we show it for a model with  $h = 0.5$  and  $\Lambda = 0$ . From such curve, the isoprobability contours can be readily obtained.

They encompass volumes corresponding to 68.3%, 95.4%, 99.7% of the total volume below the 2-dimensional curve, respectively, and will be called 1–2–3 $\sigma$  contours, in the sequel.

We found a fairly regular behaviour of  $\ln(\mathcal{L})$  which can be expressed through a third degree polynomial in  $x \equiv n - n^o$  and  $y \equiv a_{10} - a_{10}^o$ ; here  $n^o$  and  $a_{10}^o$  yield the peak position. More in detail, our fitting formula reads:

$$-2 \ln \mathcal{L}' = P_1 x^2 + P_2 xy + 5.9y^2 + P_3 x^2 y + P_4 y^3 + P_5 xy^2 - 0.78y^3. \quad (22)$$

In Table 1 we give the values of the best-fit values of the parameters  $P_i$  ( $i = 1, \dots, 5$ ),  $n^o$  and  $a_{10}^o$  for the models of the lattice. The expression (22), together with the values in Table 1, outlines that substantial deviation from a Gaussian behaviour in the error distribution are present; however, to put them under control, up to the 3 $\sigma$  level, it is sufficient to use third degree polynomials. The quality of the fits obtained in this way can be appreciated from Fig. 2, where we show how the 1–2–3 $\sigma$  contours obtained from model analysis and fitting formula agree, for a set of typical cases. Residual discrepancies, visible for the 3 $\sigma$  contours, correspond to overall likelihood shifts  $\sim 10^{-6}$ .

The fact that the expected non-Gaussian behaviour is so simply fitted, is not the only finding of this work. In fact, we also find that all the coefficients  $P_i$ ,  $n^o$  and  $a_{10}^o$  in the expression (22), can be fairly approximated using a single interpolating expression, as simple as

$$a + b\Omega_\Lambda^S + c\Omega_\Lambda^{2S}. \quad (23)$$

In Table 3 we give the values of the interpolating coefficients  $a$ ,  $b$ ,  $c$  and  $S$ . In Fig. B, we show how our fitting formula meets the  $P_i$  values (in two typical cases),  $n^o$  and  $a_{10}^o$  obtained for the various models.

In order to validate our algorithm, we produced 120 CMBR sky realizations for cosmological models with assigned  $a_{10} = 6.93 \mu K$ ,  $\Omega_\Lambda = 0$  and  $n = 1.00$ , simulated their observation with COBE–DMR, and applied our algorithm to determine the model likelihood in the space spanned by  $a_{10}$ ,  $\Omega_\Lambda$  and  $n$ . The simulated CMBR sky was produced using an algorithm based on the technique suggested by Muciaccia, Natali & Vittorio (1997). The  $C_l$  coefficients required were generated using CMBFAST. The spectrum was then multiplied

$h$	$\Omega_\Lambda$	$P_1$	$P_2$	$P_3$	$P_4$	$P_5$	$n^\circ$	$a_{10}^\circ/\mu K$
0.7	0.8	9.93	1.14	2.24	-1.53	1.72	1.1711	6.1579
	0.7	12.31	0.50	2.36	-0.71	1.92	1.1149	6.2173
	0.6	14.68	-0.123	2.17	0.66	2.07	1.0831	6.2547
	0.4	17.46	-1.014	1.38	3.28	2.28	1.0550	6.2927
	0.2	18.62	-1.44	0.89	4.59	2.37	1.0489	6.3073
0.6	0.7	12.43	0.42	2.33	-0.61	1.92	1.1138	6.2176
	0.6	14.69	-0.168	2.14	0.73	2.07	1.0852	6.2552
	0.4	14.69	-1.04	1.36	3.22	2.28	1.0597	6.2944
	0.2	14.69	-1.46	0.88	4.49	2.36	1.0550	6.3099
0.5	0.4	17.41	-1.052	1.36	3.27	2.28	1.0605	6.2941
	0.3	18.08	-1.300	1.06	4.02	2.33	1.0574	6.3039
	0.2	18.45	-1.458	0.89	4.47	2.36	1.0574	6.3102
	0.1	18.61	-1.540	0.77	4.69	2.38	1.0598	6.3136
	0.0	18.33	-1.58	0.7	4.5	2.38	1.0647	6.3138

Table 1: Values of parameter to fit the likelihood function, see eq. (22). Such values are reported as an intermediate step of our work and mostly to show the residual small dependence on  $h$  of the fitting constants. Such dependence will be neglected in the final fitting expression.

by the COBE–DMR experiment window function. COBE–DMR features were used also to define pixels and pixel noise variance. Using such fictitious data, we searched the top–likelihood point for all models in the  $n$ – $a_{10}$  plane, using the same algorithm applied to COBE–DMR data. The effect of the  $20^\circ$  subtraction along the galactic plane was also tested, by searching the top–likelihood point for all models, also without galactic plane subtraction. Our algorithm recovers  $n = 1.01 \pm 0.13$  and  $a_{10} = 6.92 \mu K \pm 0.30 \mu K$  (the latter standard deviation corresponds to  $\simeq 4\%$ ). When the full sky is used, standard deviations are reduced by  $\sim 20\%$  and  $\sim 30\%$ , respectively. For the sake of comparison, let us report that a more limited test, reported by BW, who made simulated maps with purely Sachs & Wolfe input spectra, gave  $\Delta n \sim 0.26$  and a normalization discrepancy up to  $\sim 7\%$ .

We also compared our results with those cases already treated in the literature. In Table 2 we present the results of previous works on  $n$  and  $Q$ , using 4–year COBE–DMR data. The last line of the table provides our estimate, assuming a pure Sachs & Wolfe spectrum. The dispersion in the values of the table is to be attributed to different choices of the “Galactic–plane cut” and different combinations of the 3 frequencies, while results should not be affected by different data compres-

sion techniques. For each result, however, we indicate the method used by the authors.

Here we shall report some details on the comparison with the analysis of G96, on 4–year COBE–DMR data, assuming a pure Sachs & Wolfe angular spectrum, and with the outputs of BW.

In G96, a (3\*961) component signal vector was built setting together the data of the three maps at 31.5, 53 and 90 GHz. An analogous (3\*961) component noise vector is also built. Pixels only at galactic longitude above  $20^\circ$  are taken. Monopole and dipole components of each map, which are not physically relevant to the power spectrum estimation, could be exactly removed by integrating over the first four components. We performed a similar analysis using (2\*961) component vectors, based on maps at 53 and 90 GHz (the 31.5 GHz map, characterized by high noise level, was not taken into account). Results are shown in Fig. 4, where we report 1–2–3  $\sigma$  curves; the top–likelihood point we find is indicated by an empty triangle, while the G20+\* top–likelihood point (see table 2) is indicated by a filled box.

In BW, a weighted average of the signals at 53 and 90 GHz is used, as we did in this work. The signal compression technique is however quite different from the one used here. The total number of pixels they use is 3890, after all pixels below the

	$n$	$Q(\mu K)$	$Q _{n=1}(\mu K)$
G20 *	$1.22^{+0.24}_{-0.28}$	$16.71^{+3.93}_{-3.12}$	$19.40^{+1.29}_{-1.25}$
G20 + *	$1.23^{+0.23}_{-0.29}$	$15.26^{+3.93}_{-2.64}$	$18.34^{+1.25}_{-1.20}$
G30 + *	$1.23^{+0.29}_{-0.34}$	$15.18^{+4.46}_{-2.92}$	$17.82^{+1.44}_{-1.34}$
G20 + $l-g$	$1.11^{+0.38}_{-0.42}$	$16.33^{+5.18}_{-3.69}$	$17.38^{+1.77}_{-1.68}$
G30 + $l-g$	$0.79^{+0.48}_{-0.55}$	$18.63^{+7.72}_{-5.08}$	$16.57^{+1.92}_{-1.82}$
G20 + * $-g$	$1.21^{+0.24}_{-0.28}$	$15.23^{+3.69}_{-2.64}$	$17.67^{+1.25}_{-1.15}$
G30 + * $-g$	$1.24^{+0.27}_{-0.33}$	$14.80^{+4.07}_{-2.83}$	$17.34^{+1.39}_{-1.34}$
H $w$	$1.25^{+0.26}_{-0.29}$	$15.4^{+3.9}_{-2.9}$	$18.4^{+1.4}_{-1.3}$
H $w-g$	$1.23^{+0.26}_{-0.27}$	$15.2^{+3.6}_{-2.8}$	$17.8^{+1.3}_{-1.3}$
H $l$	$1.00^{+0.40}_{-0.43}$	$17.2^{+5.6}_{-4.0}$	$17.2^{+1.9}_{-1.7}$
B $w2$	$1.18 \pm 0.28$	16.2	$18.7 \pm 1.26$
T20 $w2$	$1.21^{+0.35}_{-0.42}$	$14.7^{+5.56}_{-3.36}$	$17.1 \pm 1.5$

Table 2: Best fit values of  $n$  and  $Q$  (quadrupole) from this and previous works; the best-fit values of  $Q$  for  $n = 1$  are also given. In the first column we give the initial of the first author (G for G96, H for Hinshaw et al. 1996, B for BW and T for the present work). The number after G indicates the width of the cut around the galactic equator and, in general, notation is the same as in G96. Results by other authors are obtained by operating the so-called customary cut suggested by Bennet et al. (1996). The letter  $w$  states that results were obtained through a weighted average of the 6 maps (3 frequencies, 2 channels);  $w2$  indicates that only 4 maps were used, neglecting 31.5 GHz outputs;  $l$  indicates that a linear combination of results at various frequencies was done, taking coefficients able to cancel the contribute from free-free galactic emission;  $-g$  indicates that a correction for foregrounds was done; results obtained considering separately results at 3 frequencies are marked with \* (961+961+961 component vectors).

	$a$	$b$	$c$	$S$
$P_0$	8.34	0	-8.4	1.89
$P_1$	18.35	4.1	-19.5	1.14
$P_2$	-1.574	4.58	0	2.30
$P_3$	0.74	7.4	-8.4	2.54
$P_4$	4.66	-22.3	20	2.96
$P_5$	2.383	-1.19	0	2.64
$n^\circ$	1.06	-0.09	0.38	1.9
$a_{10}^\circ/\mu K$	6.312	-0.1	-0.2	2

Table 3: Best-fitting values of parameters in eq. (23)

“custom-cut”, described by Bennet et al. (1996), are removed.

The level of consistency between this work and BW can be appreciated in Fig. 5, where the likelihood distributions on the spectral index  $n$ , found by us and BW, are compared. As far as the distribution on  $n$  is concerned, we reproduce even minor features visible in previous outputs. On the contrary, our  $a_{10}$  values tend to be slightly smaller and the discrepancy from BW amounts to  $\sim 0.64\mu K$ .

It may be also interesting to compare our 1–2–3 $\sigma$  likelihood contours with likelihood contours obtainable from BW. It ought to be noticed that working out such contours from BW is far from trivial, as one has to translate their  $D'$  and  $D''$  parameters into  $n$  and  $\Omega_\Lambda$  values and this requires a significant numerical effort. Furthermore, the peak likelihood curve, at various  $n$  values, obtained by BW, shows features indicating a non-Gaussian behaviour in respect to  $n$ . In the  $a_{10}$  direction, instead, we have just the information that 1- $\sigma$  errors (casual) are  $\sim 7\%$  and only can we assume a Gaussian behaviour.

However, using such information, it is possible to work out 1–2–3 $\sigma$  likelihood contours. In Fig. 6 we compare our and BW curves (thick and dashed lines, respectively), after displacing BW along the  $a_{10}$  axis, so to have coincident top likelihood points. Those interested in likelihoods extrapolated from BW results, for the case  $\Omega_\Lambda = 0$ ,  $h = 0.5$ , can work them out from Fig. 6, shifting the  $a_{10}$  axis by  $0.64\mu K$ .

The main interest of this figure, however, concerns the actual distribution of the likelihood, once the non-Gaussian behaviour is fully taken into account. Fig. 6 confirms that the distributions along  $n$ , in this and BW analyses, are pretty similar. The distributions along  $a_{10}$ , instead, are different, as is expected. Substantial discrepancies already exist at 1- $\sigma$  level and they are asymmetrical in the two directions of the  $a_{10}$  axis.

#### 4. PS predictions and a numerical algorithm

In the preparation of this work, as previously outlined, we have extensively used the public program CMBFAST. Besides of the transfer function  $\mathcal{T}(k)$ , this program provides the angular spectra  $C_l$  (for temperature fluctuations and polarization),

normalizing all results and providing the model likelihood on the basis of BW relations. As previously outlined, this implies that, for each model, the normalization corresponding to the best-fit to COBE-DMR 4-year data is selected; the model likelihood provided by CMBFAST is the one which corresponds to such best fit.

Making use of the transfer function, a fair deal of large scale observables can be predicted. For instance, using the Press & Schechter (PS) approach, one can evaluate the expected number density of galaxy clusters. As previously outlined, this is a fair example of why one needs to go beyond the best-fit normalization.

Using the fitting formulae worked out in the previous section, we have therefore built a routine, which may be appended to CMBFAST, to replace to BW single normalization with possible normalizations for top likelihood and at the 1-2-3 $\sigma$  limits (this routine is available on SPORt web-page, <http://sport.tesre.bo.cnr.it/>). Likelihood estimates are also suitably provided to compare different models, even with different normalizations.

## 5. Conclusions

The main results of this work are: (i) The expression (22) of the 2-dimensional interpolating “curve” yielding the likelihood distribution, for models with given  $\Lambda$ , when varying  $a_{10}$  and  $n$ . It is important to stress that, although the likelihood distribution is clearly non-Gaussian, all deviations from a Gaussian behaviour are fully under control when cubic terms are added. (ii) The expression (22) is then implemented by the interpolating expressions of the  $P_i$  coefficients, given by eq. (23); here again, besides of outlining its practical use in association with Table 3 parameter values, the reader’s attention is to be attracted to its simplicity. Notice that, given the values of the 4 parameters  $a$ ,  $b$ ,  $c$  and  $S$ , our expressions provide the likelihood distribution for any critical  $\Lambda$  model in the  $a_{10}, n$  plane. That this likelihood is readily obtainable, for such a wide range of cases, just assigning a few numerical values, is one of the results of this work.

These results can be completed by an expression allowing to compare different  $\Lambda$  models, in the point of the  $a_{10}, n$  plane where they reach top

likelihood. In Fig. 7 the top likelihood of models is plotted against  $\Omega_\Lambda$ . The *best-fit* curve shown in Fig. 7 has equation:

$$\mathcal{L} = a + b\Omega_\Lambda^S + c\Omega_\Lambda^{2S} \quad (24)$$

with  $a = 0.98$ ,  $b = 0.34$ ,  $c = -1.24$ ,  $S = 1.42$ . This expression is quite similar to eq. (23), yielding the  $\Omega_\Lambda$  dependence of the coefficients  $P_i$ .

As above outlined, the class of models discussed here was previously treated also by BW, whose results also concerned models with non-critical density. If we consider only critical  $\Lambda$ CDM models, seemingly favoured by current observations, the likelihood distribution in respect to the spectral index  $n$ , found in BW, is the same as the one found in this work. In respect to normalization, instead, we find top likelihood for values smaller by  $\sim 7\%$  (see fig. 6), in respect to BW. By itself this is not surprising, owing to various differences between ours and BW analyses: first of all, the different techniques adopted to subtract the galactic equatorial band. Such percentage can be also considered the typical discrepancy among the amplitudes that different authors obtain from COBE-DMR data analysis, and the size of the 1- $\sigma$  errorbar for the amplitude.

Such size of errorbar had already been suggested by BW, although no justification of their finding is reported in their article. Besides of a detailed treatment of error analysis, in this work we provide errors up to 3- $\sigma$ , in the 3-dimensional space spanned by amplitude, spectral index and  $\Lambda$ , fully accounting for their deviation from a Gaussian behaviour.

The above uncertainty of 7% makes perhaps redundant the information on non-Gaussian behaviour at the 1- $\sigma$  level, which implies corrections smaller than 7%. However, if a likelihood distribution above 1- $\sigma$  is needed, the results of this work are to be applied; furthermore, above 1- $\sigma$ , deviation from Gaussian behaviour approach errorbar size. A typical case when likelihood distributions above 1- $\sigma$  are needed is when COBE likelihood is to be considered together with the likelihood distribution worked out from other experiments. In this case, the joint likelihood might well reach its top for a model discrepant more than 1- $\sigma$  from COBE maximum likelihood, but, even if not so, distributions above 1- $\sigma$  are to be considered to perform a complete analysis.



As above outlined, our results hold almost independently of the value of the Hubble parameter  $H$ . Its impact on  $C_l$  up to  $l = 30$  is known to be quite limited, and we tested that, in the range 50–70 km/s/Mpc, we do not need to specify its value. The same can be said for the baryonic content of the model. Of course, both  $H$  and  $\Omega_b$  affect  $C_l$  at greater  $l$  values. We have not checked our output against a variation of the nature of dark matter. If a significant massive neutrino contribution to dark matter is present (density parameter  $\Omega_h$ ), some changes of  $C_l$  are expected for  $l \sim 200$ . Such changes are however rather small (Dodelson et al. 1996), unless neutrinos have a very late derelativization. The situation might be different if hot–dark–matter with non–thermal distribution is considered (*volatile* models; see Pierpaoli & Bonometto, 1999). In any case, however, the impact on  $C_l$  of a hot (or *volatile*) component, down to  $l \sim 30$ , is expected to be even smaller than the one arising from  $\Omega_b$  shifts. Hence, our fitting relations can be safely used for any value of  $H$ ,  $\Omega_b$  and for any reasonable value of  $\Omega_h$  originating from massive neutrinos.

## A. Appendix A

The sky temperature measured in a direction  $\hat{n} \equiv \theta, \phi$  is a convolution of the temperatures around ( $\hat{n}$ ) with the beam pattern. Temperatures are then averaged inside each pixel area. Let then  $w^{pix}(\theta, \phi)$  be the filter function, that models the pixel shape. Assuming it to be symmetric around the polar axis (that we choose in the  $\theta$  direction),  $w^{pix}$  depends only on the angular coordinate  $\theta$  and can be expanded in Legendre polynomials; the coefficients of the expansion then read:

$$w_l^{pix} = \frac{\int_0^\pi d\theta \sin \theta w^{pix}(\theta) P_l(\cos \theta)}{\int_0^\pi d\theta \sin \theta w^{pix}(\theta)}. \quad (\text{A1})$$

For COBE pixelization  $w^{pix}$  is a circular top-hat window with angular area  $\Omega_{pix} = 4\pi/6144$ ; let then  $\bar{\theta}$  be such that

$$\int_0^{2\pi} d\phi \int_0^{\bar{\theta}} d\theta = \Omega_{pix}, \quad (\text{A2})$$

then the eq (A1) becomes

$$\begin{aligned} w_l^{pix} &= -\frac{2\pi}{\Omega_{pix}} \int_1^{\cos \bar{\theta}} dx P_l(x) = -\frac{2\pi}{\Omega_{pix}} \int_1^{\cos \bar{\theta}} dx \frac{1}{2^l l!} \frac{d^l (x^2 - 1)^l}{dx^l} = \\ &= -\frac{2\pi}{\Omega_{pix}} \frac{1}{2^l l!} \int_1^{\cos \bar{\theta}} dx \frac{d}{dx} \left[ \frac{d^{l-1} (x^2 - 1)^l}{dx^{l-1}} \right] = -\frac{2\pi}{\Omega_{pix}} \frac{1}{2^l l!} \left[ \frac{d^{l-1} (x^2 - 1)^l}{dx^{l-1}} \right]_1^{\cos \bar{\theta}}. \end{aligned} \quad (\text{A3})$$

The values of  $w_l^{pix}$  are reported in the table below.

## B. Appendix B

By integrating the likelihood  $\mathcal{L}$  over the first 4 components of the vector  $\mathbf{c}$ , we can remove the contribution of the monopole and dipole terms. Such integration can be easily performed in the case of Gaussian distributions.

In fact, let us rewrite the expression of

$$\mathcal{L}(c_\mu) = \frac{1}{\sqrt{(2\pi)^N \det \mathbf{M}}} \exp[-(1/2) \mathbf{c}^T \mathbf{M}^{-1} \mathbf{c}], \quad (\text{B1})$$

using a greek index for the components from 1 to 4, and  $x$  or  $y$  for the components from 5 to 961. The integral of eq. (B1) reads then

$$\int dc_\mu \mathcal{L}(c_\mu) = \frac{1}{\sqrt{(2\pi)^N \det \mathbf{M}}} \int dc_\mu \exp \left( -\frac{1}{2} c_\mu M_{\mu\nu}^{-1} c_\nu - \frac{1}{2} c_x M_{xy}^{-1} c_y - c_\mu M_{\mu x}^{-1} c_x \right). \quad (\text{B2})$$

$l$	$w_l^{pix}$	$l$	$w_l^{pix}$	$l$	$w_l^{pix}$	$l$	$w_l^{pix}$	$l$	$w_l^{pix}$	$l$	$w_l^{pix}$
1	0.9998	6	0.9966	11	0.9893	16	0.9780	21	0.9629	26	0.9439
2	0.9995	7	0.9954	12	0.9873	17	0.9753	22	0.9594	27	0.9397
3	0.9990	8	0.9941	13	0.9853	18	0.9724	23	0.9557	28	0.9353
4	0.9984	9	0.9927	14	0.9830	19	0.9694	24	0.9519	29	0.9308
5	0.9976	10	0.9911	15	0.9806	20	0.9662	25	0.9480	30	0.9262

Table 4: COBE pixelization function values; see text.

Let be  $J_\mu \equiv M_{\mu x}^{-1} c_x$ , then

$$\begin{aligned} \int dc_\mu \mathcal{L}(c_\mu) &= \frac{1}{\sqrt{(2\pi)^N \det \mathbf{M}}} \exp\left(-\frac{1}{2} c_x M_{xy}^{-1} c_y\right) \times \\ &\times \int dc_\mu \exp\left(-\frac{1}{2} c_\mu M_{\mu\nu}^{-1} c_\nu - 2c_\mu J_\mu\right). \end{aligned} \quad (\text{B3})$$

Let then be  $\tilde{c}_\mu = c_\mu + b_{\mu\sigma}$ , where  $b_{\mu\sigma}$  is a generic matrix ( $4 \times 4$ ) independent from  $c_\mu$ ; using  $\tilde{c}_\mu$  as integration variables, the exponent in the integration becomes

$$\begin{aligned} c_\mu M_{\mu\nu}^{-1} c_\nu + 2c_\mu J_\mu &= (\tilde{c}_\mu - b_{\mu\sigma}) J_\sigma M_{\mu\nu}^{-1} (\tilde{c}_\nu - b_{\nu\tau} J_\tau) + \\ &+ 2(\tilde{c}_\mu - b_{\mu\sigma}) J_\mu = \tilde{c}_\mu M_{\mu\nu}^{-1} \tilde{c}_\nu - b_{\mu\sigma} J_\sigma M_{\mu\nu}^{-1} \tilde{c}_\nu + \\ &- \tilde{c}_\mu M_{\mu\nu}^{-1} b_{\nu\tau} J_\tau + b_{\mu\sigma} J_\sigma M_{\mu\nu}^{-1} b_{\nu\tau} J_\tau + 2\tilde{c}_\mu J_\mu - 2J_\mu b_{\mu\sigma} J_\sigma. \end{aligned} \quad (\text{B4})$$

If  $\mathbf{b}$  is the inverse of the ( $4 \times 4$ ) matrix  $(M^{-1})_{\mu,\nu}$ , the eq. (B) simplifies into

$$\begin{aligned} c_\mu M_{\mu\nu}^{-1} c_\nu + 2c_\mu J_\mu &= \tilde{c}_\mu M_{\mu\nu}^{-1} \tilde{c}_\nu - J_\nu \tilde{c}_\nu - J_\mu \tilde{c}_\mu + J_\mu b_{\mu\sigma} J_\sigma + \\ &+ 2\tilde{c}_\mu J_\mu - 2J_\mu b_{\mu\sigma} J_\sigma = \tilde{c}_\mu M_{\mu\nu}^{-1} \tilde{c}_\nu - J_\mu b_{\mu\sigma} J_\sigma. \end{aligned} \quad (\text{B5})$$

Henceforth, performing the integration, we have

$$\begin{aligned} \int dc_\mu \mathcal{L} &= \frac{1}{\sqrt{(2\pi)^N \det \mathbf{M}}} \exp\left[-\frac{1}{2} (c_x M_{xy}^{-1} c_y + J_\mu b_{\mu\sigma} J_\sigma)\right] \int dc_\mu \exp\left(-\frac{1}{2} \tilde{c}_\mu M_{\mu\nu}^{-1} \tilde{c}_\nu\right) = \\ &= \frac{1}{\sqrt{(2\pi)^N \det \mathbf{M}}} (2\pi)^2 \frac{1}{\sqrt{(\det \mathbf{b}^{-1})}} \exp\left[-\frac{1}{2} (c_x M_{xy}^{-1} c_y + c_x M_{x\mu}^{-1} b_{\mu\sigma} M_{\sigma y}^{-1} c_y)\right] = \\ &= \frac{1}{\sqrt{(2\pi)^{N-4} \det \tilde{\mathbf{M}}}} \exp\left[-\frac{1}{2} (c_x \tilde{M}_{xy}^{-1} c_y)\right]; \end{aligned} \quad (\text{B6})$$

the new covariance matrix  $\tilde{\mathbf{M}}$  has  $((N-4) \times (N-4))$  dimension.

Hence, the integration of the first four components of the vector  $\mathbf{c}$  is equivalent to replace the matrix  $\mathbf{M}$  with  $\tilde{M}_{xy} = M_{xy}^{-1} + M_{x\mu}^{-1} b_{\mu\sigma} M_{\sigma y}^{-1}$  (and  $N$  with  $N-4$ ) in eq (B1).

## REFERENCES

- Bennett, C.L., et al. 1994, ApJ, 436, 423
- Bennett, C.L., et al. 1996, ApJ, 646, L1
- Bond, J.R. & Efstathiou, G., 1987, MNRAS, 226, 665
- Bond, J.R., 1995, Phys. Rev. Lett., 74, 4369
- Bonometto, S.A. & Pierpaoli, E., 1998, NewA., 3, 391
- Bunn, E.F. & Sugiyama, N., 1995, ApJ, 446, 49
- Bunn, E.F. & White, M., 1997, ApJ, 480, 6 (BW)
- Contaldi, C.R., Ferreira, P.G., Magurijo, J. & Górski, K.M., 2000, ApJ, 534, 25
- de Bernardis, P., et al. 2000, Nature, 404, 995
- Dodelson, S., Gates, E. & Stebbins, A., 1996, ApJ, 467, 10
- Eke, V.R., Cole, S. & Frenk, C.S., 1996, MNRAS, 282, 263
- Eke, V.R., Cole, S., Frenk, C.S., & Henry, J.P., 1998, MNRAS, 298, 1145
- Ferreira, P.G., Magurijo, J. & Górski, K.M., 1998, ApJ, 503, L1
- Girardi, M., Borgani, S., Giuricin, G., Mardirossian, F., & Mezzetti, M., 1998, ApJ, 506, 45
- Górski, K.M., 1994, ApJ, 430, L85 (G94)
- Górski, K.M., Hinshaw, G., Banday, A.J., Bennett, C.L., Wright, E.L., Kogut, A., Smoot, G.F. & Lubin, P.M., 1994, ApJ, 430, L89
- Górski, K.M., Banday, A.J., Bennett, C.L., Hinshaw, G., Kogut, A., Smoot, G.F., & Wright, E.L., 1996, ApJ, 464, L11 (G96)
- Górski, K.M., "Microwave Background Anisotropies", proceedings of the XVIth Moriond Astrophysics Meeting, Editions Frontieres, p.77; astro-ph/9701191
- Hanany, S., et al., 2000, astro-ph/0005123
- Hinshaw, G., Banday, A.J., Bennett, C.L., Górski, K.M., Kogut, A., Smoot, G.F., & Wright, E.L., 1996, ApJ, 464, L17
- Muciaccia, P.F., Natoli, P. & Vittorio, N., 1997, ApJ, 488, L63
- Novikov, D., Feldman, H. & Shandarin, S., 1998, astro-ph/9809238
- Pando, J., Valls-Gabaud & Fang, L.Z., 1998, Phys. Rev. Lett., 81, 4568
- Perlmutter, S., et al. 1999, ApJ, 517, 565
- Pierpaoli, E. & Bonometto, S.A., 1999, MNRAS, 305, 425
- Riess, A.G., et al. 1998, AJ, 116, 1009
- Sachs, R.K. & Wolfe, A.M., 1967, ApJ, 147, 73
- Seljak, U. & Zaldarriaga, M., 1996, ApJ, 469, 437
- Smoot, G.F., et al. 1992, ApJ, 396, L1
- Stompor R., & Górski, 1994, ApJ 422, L41
- Stompor, R., Górski, K.M. & Banday, A.J., 1995a, MNRAS, 277, 1225
- Stompor, R., Górski, K.M. & Banday, A.J., 1995b, astro-ph/9502035
- Tegmark, M. & Bunn, E.F., 1995, ApJ, 455, 1
- Tegmark, M., 1997, Phys. Rev. D55, 5895; astro-ph/9611174
- Tegmark, M. & Hamilton, A., 1997, astro-ph/9702019
- Wright, E.L., Smoot, G.F., Kogut, A., Hinshaw, G., Tenorio, L., Lineweaver, C., Bennett, C.L. & Lubin, P.M., 1994, 420, 1
- Wright, E.L., Smoot, G.F., Bennett, C.L. & Lubin, P.M., 1994, 436, 443
- Wright, E.L., Bennett, C.L., Górski, K.M., Hinshaw, G. & Smoot, G.F., 1996, ApJ, 464, L21

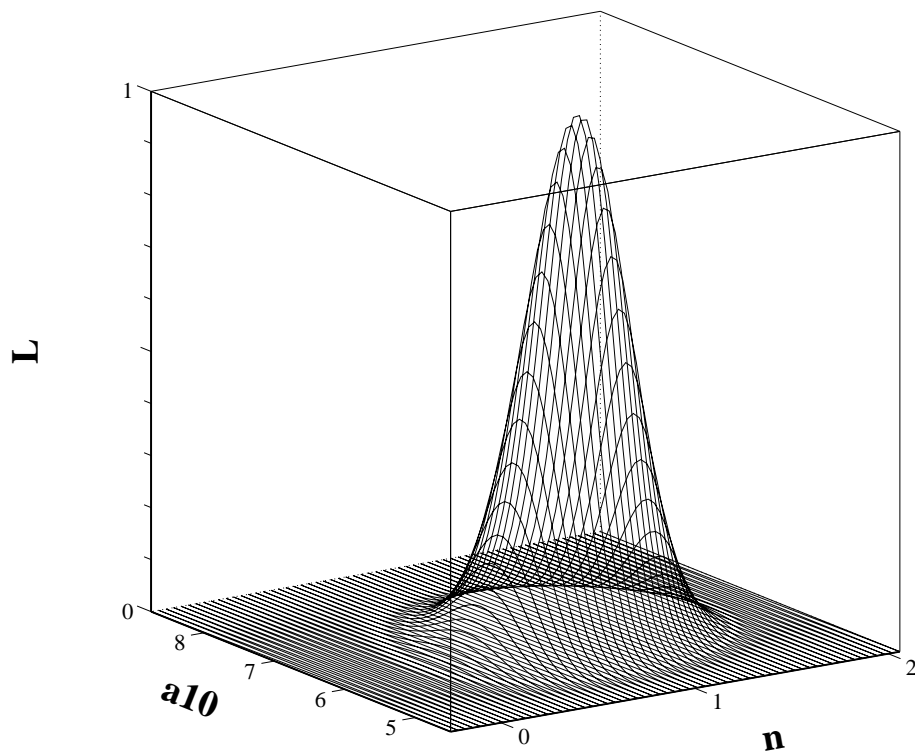


Fig. 1.— Likelihood function for  $\Omega_\Lambda = 0$  and  $h = 0.5$ ;  $a_{10}$  is expressed in  $\mu K$ .

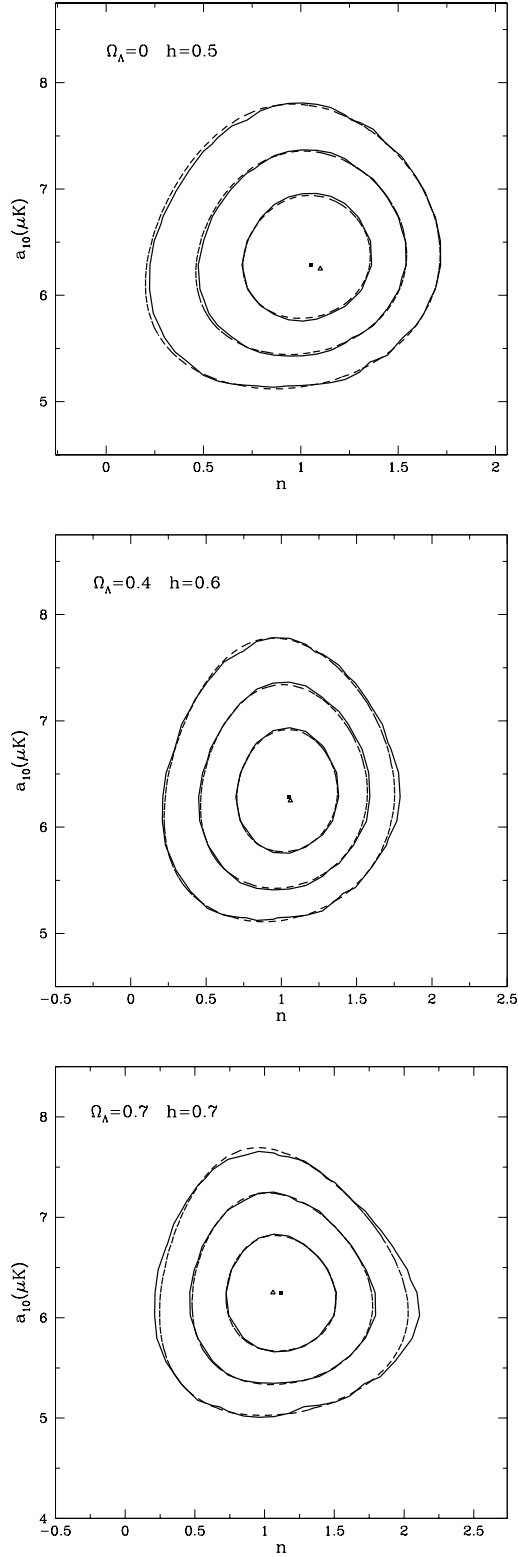


Fig. 2.— Examples of comparison between the 1–2–3 $\sigma$  confidence levels and likelihood peaks directly obtained from the likelihood function (continuous lines, filled box) and the contours obtained using the fitting formula, eq. (22) (dashed lines, empty triangles).

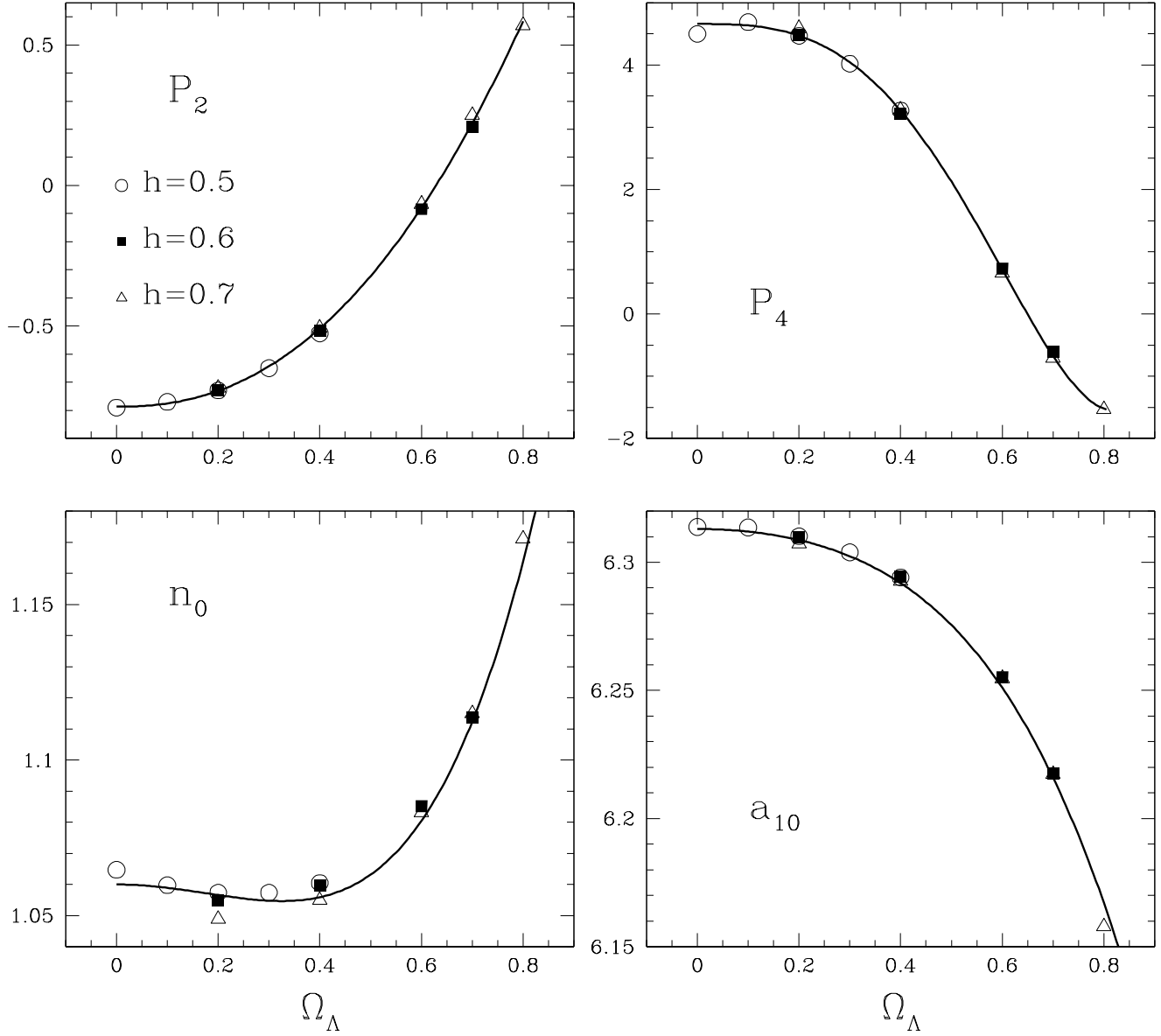


Fig. 3.— Examples of the fits between  $n^0$ ,  $a_{10}^0$  and the parameters  $P_i$  and the analytic expression 23. Different symbols are related to the values of  $h$ . Discrepancies between parameters and fitting expression are  $< 1\%$ .

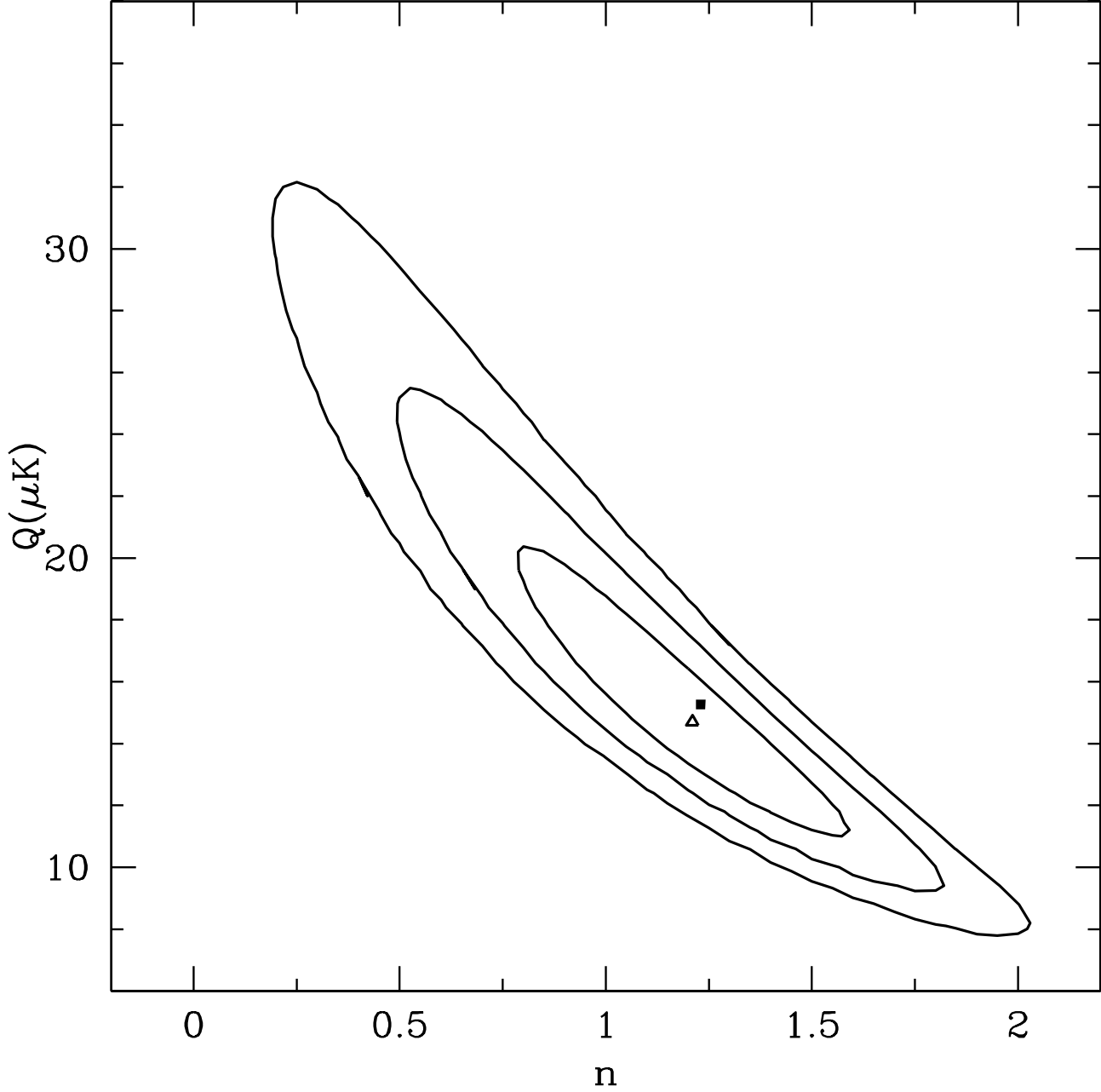


Fig. 4.— The 1-2-3 $\sigma$  confidence levels on  $Q$ - $n$  plane from 4-years COBE data, using a Sachs & Wolfe spectrum. The empty triangle is the top likelihood point we obtain. For the sake of comparison, the filled box is the top likelihood point obtained in G20+\* (see text).



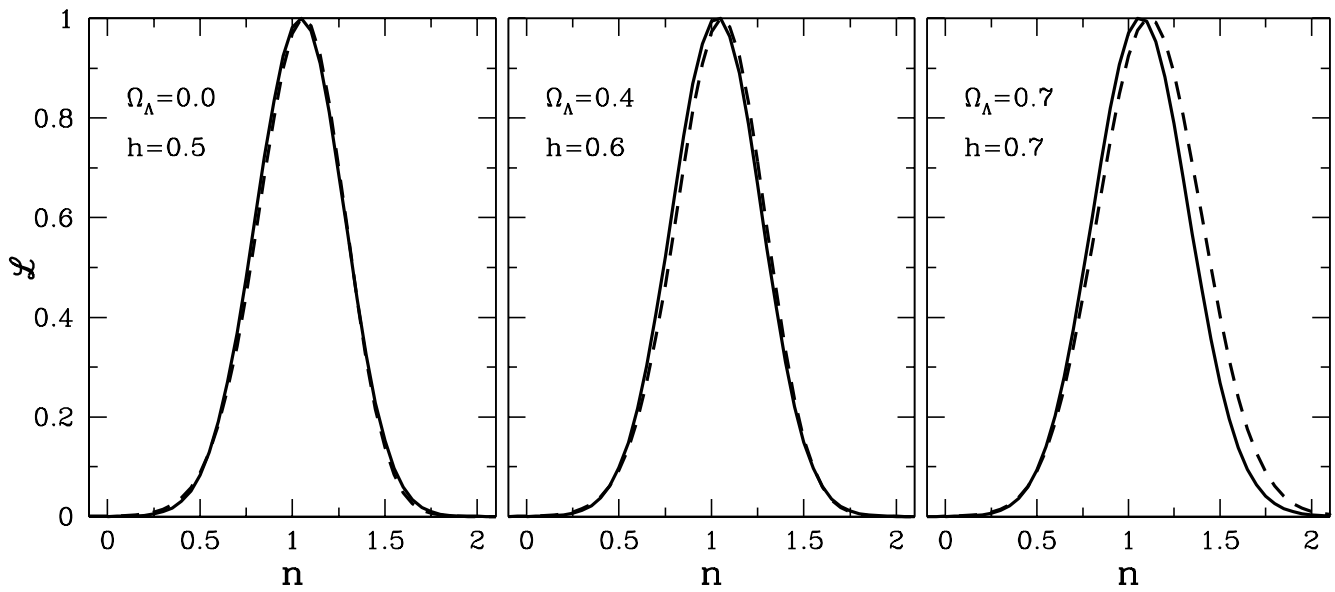


Fig. 5.— Likelihood distribution against  $n$  from BW (dashed line) and our work (continuous line).

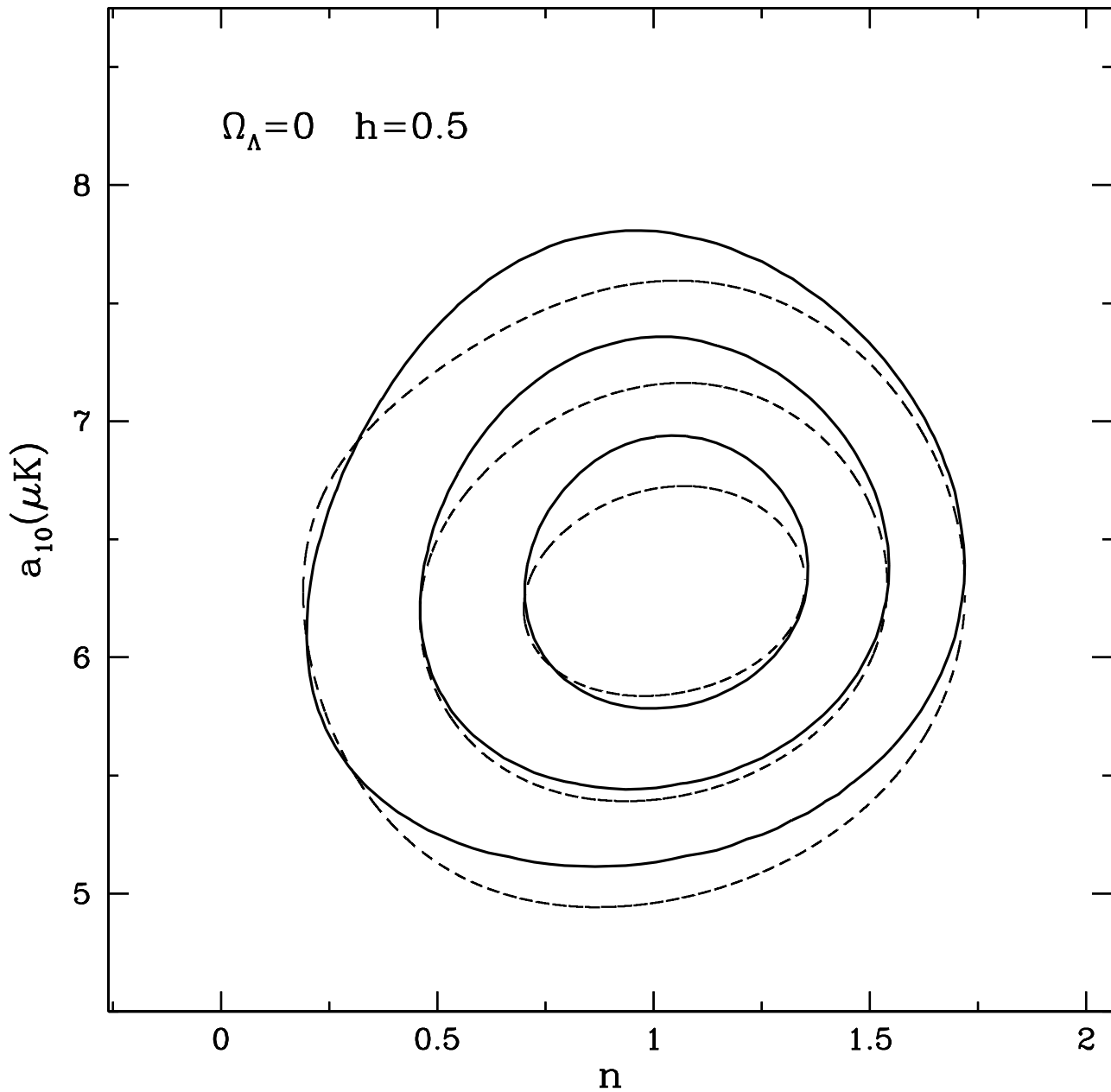


Fig. 6.— Confidence contours are shown for a model with  $\Omega_\Lambda = 0$  and  $h = 0.5$  (thick lines) and compared with confidence contours obtainable from BW (dashed lines), displaced to overlap top likelihood points. This figure exhibits the effect of taking suitably into account the deviations from a Gaussian behaviour.

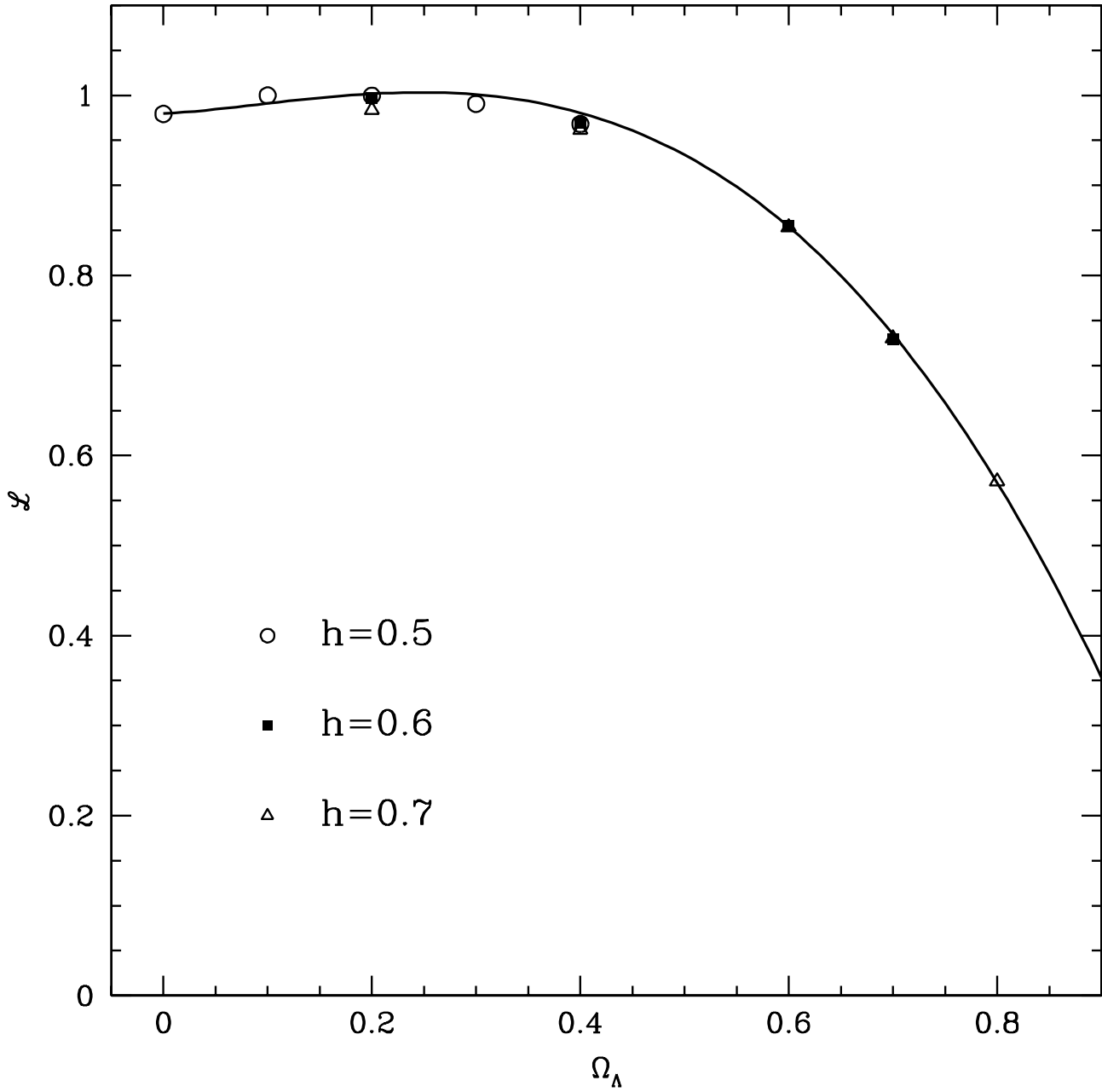


Fig. 7.— Top values of the likelihood for models with different  $\Omega_\Lambda$ . The values of  $a_{10}$  and  $n$  giving such likelihood are obtained from expression 24.